Topological transitions in fluid lipid vesicles: activation energy and force fields

Matteo Bottacchiari
Sapienza University of Rome https://orcid.org/0000-0003-3689-8847
Mirko Gallo
Sapienza University of Rome
Marco Bussoletti
Sapienza University of Rome https://orcid.org/0000-0002-9181-1284
Carlo Massimo Casciola (carlomassimo.casciola@uniroma1.it)
Sapienza University of Rome https://orcid.org/0000-0001-8795-4517

Article

Keywords:

Posted Date: May 12th, 2022

DOI: https://doi.org/10.21203/rs.3.rs-1533273/v1

Additional Declarations: There is **NO** Competing Interest.

Version of Record: A version of this preprint was published at Communications Physics on November 12th, 2022. See the published version at https://doi.org/10.1038/s42005-022-01055-2.

Topological transitions in fluid lipid vesicles: activation energy and force fields

Matteo Bottacchiari, Mirko Gallo, Marco Bussoletti and Carlo Massimo Casciola*
Department of Mechanical and Aerospace Engineering,
Sapienza Università di Roma, Rome, Italy
(Dated: April 29, 2022)

Topological transitions of fluid lipid membranes are fundamental processes for cell life. For example, they are required for endo- and exocytosis or to enable neurotransmitters to cross the neural synapses. Inspired by the idea that fusion and fission proteins could have evolved in Nature in order to carry out a minimal work expenditure, we evaluate the minimal free energy pathway for the transition between two spherical large unilamellar vesicles and a dumbbell-shaped one. To address the problem, we propose and successfully use a Ginzburg-Landau type free energy, which allows us to uniquely describe without interruptions the whole, full-scale topological change. We also compute the force fields needed to overcome the involved energy barriers. The obtained forces are in excellent agreement, in terms of intensity, scale, and spatial localization with experimental data on typical fission protein systems, whereas they suggest the presence of additional features in fusion proteins.

* carlomassimo.casciola@uniroma1.it

I. INTRODUCTION

In this work, we develop, numerically demonstrate, and use a Ginzburg-Landau type free energy [1] to study fission and fusion events of large unilamellar vesicles (LUVs) formed by a fluid lipid bilayer. The traditional approach to dealing with such systems is based on the Canham-Helfrich description, whereby the membrane is treated as a geometrical surface endowed with elastic properties. In fact, most of the experimental results concerning lipid bilayers are still today interpreted in light of this celebrated model. Its main limitation consists in the inability to account for topological changes, like those associated with fusion and fission processes. The main advantage of the approach we propose is indeed to naturally handle topological transitions.

Topological transitions of fluid lipid membranes are involved in most of the fundamental processes of cell life, like endocytosis and exocytosis. An example of such transformation is the merging of two membranes. This is the case of vesicle-vesicle fusion or viral membrane fusion. Indeed, viruses enveloped by a lipid bilayer, such as HIV, Ebola virus, influenza, measles, rabies virus, and SARS-CoV-2 can infect a target cell by fusion of their membrane with the cell plasma membrane [2, 3]. Viral infection can also occur via endocytosis, in which the plasma membrane undergoes fission to internalize the virus via an endosome. Therefore, another important topological change is membrane fission, which is also fundamental for cell division and therefore for life [4, 5]. Topological transitions of lipid membranes are of great interest not only in biology and biophysics but also in medicine and in the pharmaceutical industry. Indeed, lipid-based nanoparticles are used for drug delivery, offering many advantages including biocompatibility, bioavailability, self-assembly, and payload flexibility [6]. Micelles, closed lipid monolayers, are currently used in mRNA-vaccines against COVID-19 and many other lipid nanoparticle-mRNA applications are under clinical evaluation, e.g. for the treatment of cancer or genetic diseases [7]. Regardless of the application, all these nanoparticles are engineered to overcome the physiological barriers by exploiting topological transitions [8].

As anticipated, fluid lipid membranes can be mechanically described using the continuum approach initially introduced in [9, 10]. Such a classical elastic perspective describes a membrane as a two-dimensional surface Γ with an energy density depending on its principal curvatures. An expansion of this density up to the second-order in curvatures leads to the Canham-Helfrich Hamiltonian:

$$E_{CH}[\Gamma] = 2k \int_\Gamma (M-m)^2 \, dS + k_G \int_\Gamma G \, dS. \quad (1)$$

Here, the first term on the right-hand side is the bending energy and the second one is the Gaussian energy. M is the mean curvature of the surface, G its Gaussian curvature, m a spontaneous mean curvature that the membrane tends to adopt in absence of external forces, and k and k_G are called bending rigidity and Gaussian curvature modulus, respectively. k can be experimentally measured in different ways [11], whereas k_G is more elusive due to the celebrated Gauss-Bonnet (GB) theorem,

$$\int_\Gamma G \, dS = 2\pi\chi(\Gamma) - \int_{\partial\Gamma} k_g \, dl, \quad (2)$$

where $\chi(\Gamma)$ is the Euler characteristic of Γ and k_g is the geodesic curvature of the surface boundary $\partial\Gamma$. In the vesicles case, since they are compact surfaces without boundary, the line integral vanishes, and $\chi(\Gamma)$ becomes equal to $2-2g$, being g the genus of the surface. Therefore, the Gaussian energy term remains constant as long as no topological transitions occur, leading to the aforementioned elusive behavior of k_G. A stability argument [12] shows that $-2 < k_G/k < 0$ and in literature there is evidence [13–15] that $k_G \approx -k$. Because of the scale invariance of the Canham-Helfrich free energy, for a given topology, vesicles shapes are dictated by their reduced volume $v = V/(\pi D_{\rm ve}^3/6)$, as well as by their reduced spontaneous curvature $m_0 = mD_{\rm ve}$, where $D_{ve} = \sqrt{A/\pi}$ is the characteristic lenght of the vesicle under consideration, having area A and volume V.

The Canham-Helfrich description is thought to hold for vesicles with a characteristic length $D_{ve} \geq 40 \; l_{me}$ [16], being l_{me} the lipid bilayer thickness, which is usually about 5 nm; otherwise, higher-order terms in the energy density could make a significant contribution. Therefore, equation (1) describes vesicles larger than those simulated by means of coarse-grained molecular dynamics (MD) and dissipative particle dynamics (DPD), which have been the most widely used techniques for in silico studies of topological transitions to date [17–23]. These computer simulations, which take into account the molecular details of lipid bilayers, allow monitoring in time morphological changes of small liposomes with a size below 50 nm [24]. In many cases of interest, the vesicles sizes are considerably larger and the characteristic time of the process is so long to be inaccessible to atomistic methods. These large-sized vesicles are the target of our present study.

Most of our current understanding of membrane fusion and fission events comes from experiments. Recently, controlled fission of cell-sized vesicles by low densities of membrane-bound proteins has been reported in [25]. Other examples of fission experiments can be found in [26, 27], whereas, as regards fusion, merging of giant liposomes has been observed in [28–30], the stalk intermediate in [31], and activation energies for small liposomes fusion events have been measured in [32, 33] by means of kinetic analysis.

In the context of a Ginzburg-Landau formulation, an analog of the bending energy term was initially introduced in [34–36], leading to numerous applications, see, e.g, [37–45]. Furthermore, in [46], it has been pointed out that it is possible to retrieve topological information from such models. However, all these works do not include in the dynamics the Gaussian contribution to the free en-

ergy. As will be shown below, the inclusion of a new term accounting for such a contribution is crucial to correctly predict the physics of fusion and fission events. Indeed, in accordance with the GB theorem, the new term allows for the quantized energy jumps that significantly contribute to the free energy barriers of topological transitions. From a strictly mathematical point of view, the proposed free energy functional regularizes the Gaussian term of the Canham-Helfrich Hamiltonian, allowing the description of the process across the topological change.

Exploiting rare event techniques [47], we compute a minimal energy pathway (MEP) [48–51] and the free energy barrier between two spherical vesicles and a dumbbell-shaped one, a case recently observed in experiments [25]. We also compute the force fields needed to overcome these barriers in a straightforward manner, uniquely accounting for the force component arising from the Gaussian energy. These forces are necessary to balance the reaction resulting from the membrane (bending and Gaussian) elasticity and incompressibility, see [52] for a discussion on the difficulties in computing the bending forces using more classical approaches. The computation of the complete system of forces is expected to pave the way for exploring how the protein machineries effectively work across the full scale of vesicles.

RESULTS

Free energy functional

The classical Canham-Helfrich model succeeds in describing many aspects of the vesicle dynamics but rules out the possibility of dealing with topological changes unless unphysical surgical operations are conceived to cut and paste patches of the membrane. A viable alternative to the sharp interface description is to employ a smooth function defined on a domain Ω – the phase-field $\phi(\boldsymbol{x})$ – that discriminates between the inner and the outer environment of the vesicle assuming the limiting values ± 1 in the two regions. The $\phi(\boldsymbol{x}) = 0$ level set represents the membrane midsurface Γ. The transition between the two limiting values takes place in a narrow region whose width is controlled by a small parameter ϵ. This region will also be related to the thickness of the lipid bilayer. The main advantage of describing the membrane with such a field lies in the fact that it enables topological modifications of the membrane, allowing to address the problem of vesicle fusion and fission.

A free energy functional

$$E[\phi] = E_B[\phi] + E_G[\phi], \tag{3}$$

is associated with each field configuration, where

$$E_B[\phi] = k\,\frac{3}{4\sqrt{2}}\,\epsilon \int_\Omega \Psi_B^2\, dV, \tag{4}$$

$$\Psi_B = \nabla^2\phi - \frac{1}{\epsilon^2}(\phi^2-1)(\phi + \sqrt{2}\epsilon m)\ , \tag{5}$$

and

$$E_G[\phi] = k_G\,\frac{35}{16\sqrt{2}}\,\epsilon^3 \int_\Omega \Psi_G\, dV, \tag{6}$$

$$\begin{aligned}\Psi_G = &\frac{\boldsymbol{\nabla}|\boldsymbol{\nabla}\phi|^2\cdot\boldsymbol{\nabla}|\boldsymbol{\nabla}\phi|^2}{2} - (\boldsymbol{\nabla}|\boldsymbol{\nabla}\phi|^2\cdot\boldsymbol{\nabla}\phi)\nabla^2\phi \\ &+ |\boldsymbol{\nabla}\phi|^2\left[(\nabla^2\phi)^2 + \boldsymbol{\nabla}\phi\cdot\boldsymbol{\nabla}\nabla^2\phi - \frac{\nabla^2|\boldsymbol{\nabla}\phi|^2}{2}\right].\end{aligned} \tag{7}$$

$E_B[\phi]$ was already introduced in [34] to model the bending energy of the membrane, while $E_G[\phi]$ is the term proposed here to account for the Gaussian contribution. In Section Methods, we show that the free energy functional $E[\phi]$ recovers the Canham-Helfrich Hamiltonian, $E[\phi] \sim E_{CH}[\Gamma]$, in the sharp interface limit ($\lambda = \epsilon/D_{ve} << 1$).

Furthermore, lipid vesicles are subjected to geometrical constraints on area and enclosed volume. Indeed, since lipids are insoluble in water, the number of membrane lipids is conserved. This fact, coupled with the observation that the membrane rupture tension is very small, implies that the vesicle area A cannot substantially vary at a fixed temperature. The volume V of the vesicle is instead determined by the osmotic conditions. In order to enforce the above constraints in this phase-field context, we use suitable functionals $A[\phi]$ and $V[\phi]$ which recover

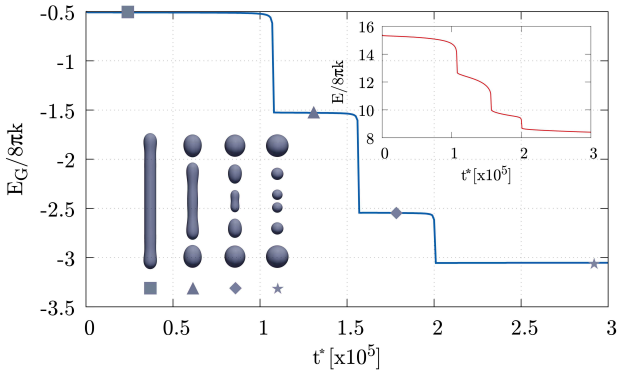

Fig. 1 Free energy evolution example. The phase-field Gaussian energy E_G during a series of scissions of a prolate shape into several spheres. The energy jumps by $-4\pi k$ for any division as prescribed by the Gauss-Bonnet theorem ($k = -k_G$). The fission process occurs due to the presence of a spontaneous curvature $m^* \approx 0.42$. Time evolution is given by the Allen-Cahn gradient flow with $M^* = 8$ (see Section Methods for more details on the dynamics, the adopted numerical scheme and dimensionless quantities). The inset shows the total energy $E = E_B + E_G$, which monotonically decreases in time, revealing the stability of the scheme. This z-axial symmetric simulation has been carried out in a $[0, 36] \times [0, 440]$ computational domain in the $r^* - z^*$ plane with a 54×660 mesh, initial $D^*_{ve} = 1/\lambda \approx 109$ and $dt^* = 4$. There is no constraint on the area, which, at the end of the simulation, differs from the initial value by approximately 6.9%. Volume is conserved with a relative error smaller than 10^{-7} with respect to its initial value.

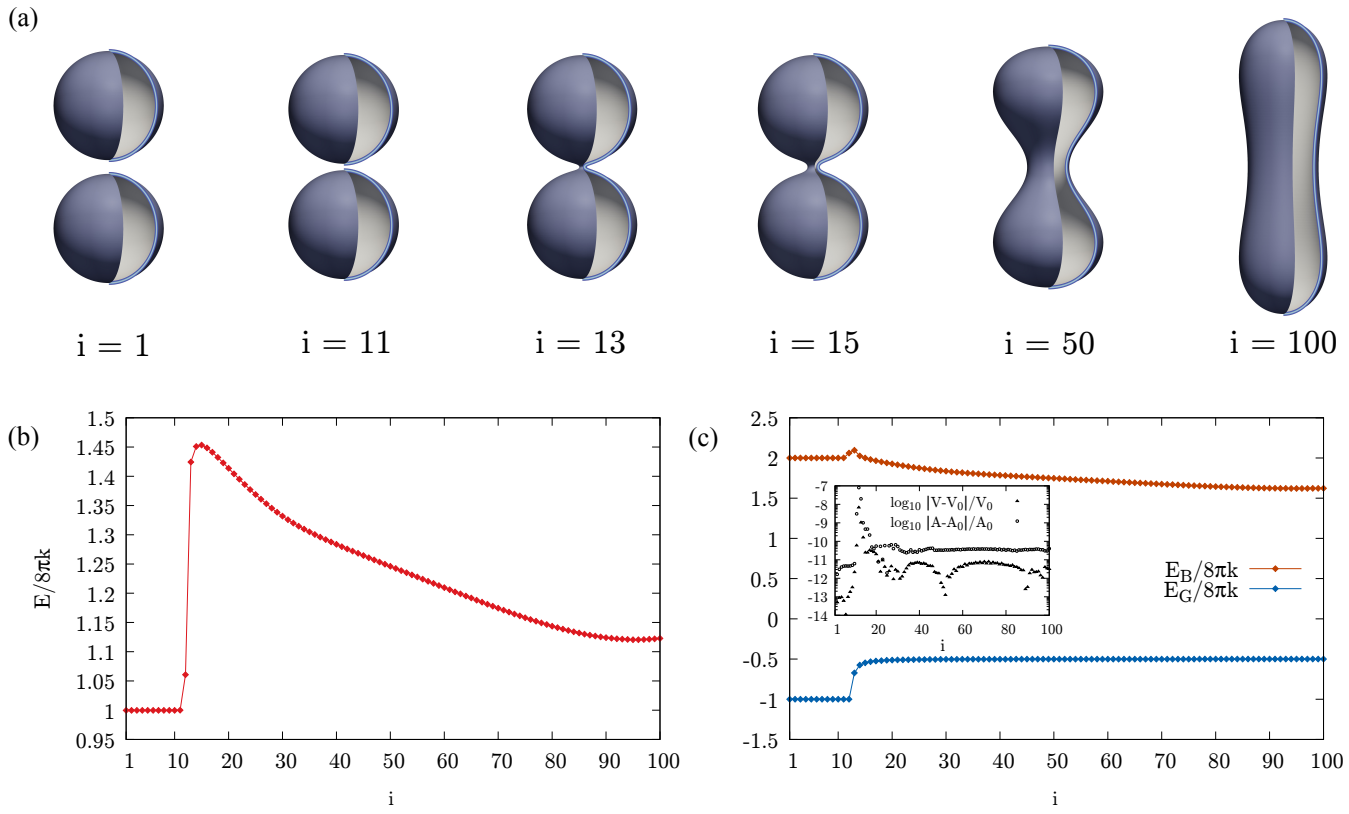

Fig. 2 The minimal free energy path. The MEP connecting two spheres of radius $R^* = 87.5$ with a dumbbell shape, $k = -k_G$. The path consists of vesicles with constant area and volume and therefore with constant reduced volume $v \approx 1/\sqrt{2}$. There is no spontaneous curvature, $m^* = 0$. This z-axial symmetric result is obtained with the string method and the new free energy functional, using a $[0, 96] \times [-245, 245]$ computational domain in the $r^* - z^*$ plane with a grid of 144×735 nodes per image, $N = 100$ images and $1/\lambda \approx 247.5$. As explained in the text, this setting leads to having $D_{ve} \approx 206$ nm. The dimensionless quantities are however useful because, far from the moment in which the topology changes, the scale invariance is expected to hold. **a** Six vesicle shapes along the minimal energy path, identified by their image number $i = (N-1)\alpha_i + 1$, being α the string parameter (equal arc-length parameterization). From right to left we can observe the fission process of the dumbbell shape into two spheres, whereas from left to right the fusion process. **b** The free energy, equation (3), along the path. Saddle point is placed between the images $i = 14$ and $i = 15$ and consists of two spherical vesicles connected by a catenoid-like neck. **c** The bending and Gaussian energy contributions to the energy along the path. The inset shows the effectiveness of the scheme in preserving vesicles area and volume. Reference values of area and volume are $A_0^* = 1.924392 \cdot 10^5$ and $V_0^* = 5.615982 \cdot 10^6$.

the vesicle area and volume, respectively, in the sharp interface limit (see Section Methods).

Throughout the paper, an asterisk will denote the dimensionless quantities obtained using ϵ as the reference length and $8\pi k$ as the reference energy. The latter is the bending energy of an isolated sphere. The typical value of the bending rigidity is $k = 20\, k_B T$, with k_B the Boltzmann constant and T the temperature. Moreover, henceforth we will assume $k_G = -k$.

As an illustrative example of the effectiveness of the approach, Figure 1 shows the Gaussian energy during a series of scissions of an unstable prolate shape into several spheres due to the presence of a spontaneous curvature, see also [53]. The evolution equation is described in Section Methods together with the adopted numerical scheme. In the same Section, the consistency of the present phase-field approach with the Gauss-Bonnet theorem is discussed. Here, it is only worth saying that the novel energy functional is able to properly capture the Gaussian energy jumps due to topological transitions.

Minimal energy pathway

In the topological transition between two spherical vesicles and a dumbbell-shaped one, which are two stable states, the system goes through a sequence of configurations $\phi_\alpha(\boldsymbol{x})$ in the space of the phase-field, identifying a path which we parameterize by the normalized arc-length $\alpha \in [0, 1]$. An MEP for this transition is a curve on the energy landscape $E[\phi]$ connecting the two stable states $\phi_{\alpha=0}(\boldsymbol{x})$ and $\phi_{\alpha=1}(\boldsymbol{x})$, respectively, and such that it is everywhere tangent to the gradient of the potential $(\partial\phi_\alpha/\partial\alpha \propto \delta E[\phi_\alpha]/\delta\phi)$, except at critical points [54]. An

initial guess of the path is discretized in a *string* made up of $N = 100$ images corresponding to $\alpha_i = (i-1)/(N-1)$. The initial guess is relaxed towards the MEP by means of the string method (see [47, 55, 56] and Section Methods) suitably accounting for the constraints of constant total surface area, equation (16), and enclosed volume, equation (17). The obtained MEP goes through a saddle point $\phi_{\alpha_c}(\boldsymbol{x})$ for the free energy, determining the transition barriers $\Delta E^{\dagger}_{0\to1} = E[\phi_{\alpha_c}] - E[\phi_{\alpha=0}]$ and $\Delta E^{\dagger}_{1\to0} = E[\phi_{\alpha_c}] - E[\phi_{\alpha=1}]$, for the forward and backward process, respectively.

Figure 2 shows the computed MEP for membranes with zero spontaneous curvature, $m = 0$. Since the phase-field ϕ reaches its limiting values ±1 with an accuracy of about 3% already at a distance of $\pm3\epsilon$ from the $\phi = 0$ membrane midsurface, we assume that $l_{pf} = 6\epsilon$ represents the thickness of the diffuse interface. In Section Methods, we show that the phase-field description recovers the Canham-Helfrich model in the limit of small $\lambda \propto \ell_{pf}/D_{ve}$. Our numerical experiments, reported in the Supplementary Information, point out that this asymptotic behavior is already achieved when $\ell_{pf}/D_{ve} >> (\ell_{me}/D_{ve})_{\max} = 1/40$, the latter being the maximum thickness-to-curvature radius ratio for which the Canham-Helfrich model is accepted [16]. Since the relative distance between approaching membrane segments is relevant during the topological transition, it is crucial that the diffuse interface width matches the bilayer thickness. This requirement fixes the scale of our system. Setting $l_{pf} = l_{me} = 5\,\mathrm{nm}$, the configurations shown in Figure 2a correspond to vesicles with $D_{ve} \approx 206\,\mathrm{nm}$, thus within the range of validity of the asymptotic Canham-Helfrich model and well beyond the current limits of atomistic approaches.

Figure 2a shows successive configurations along the MEP. Increasing/decreasing α corresponds to moving along the path in the direction of the fusion/fission (forward/backward) process, respectively. Proceeding forward, the two vesicles come closer to each other without deforming, get in touch, and merge together forming a narrow neck that expands until the final dumbbell-shaped configuration is reached. As explained in the Introduction, the equilibrium states of a vesicle are determined by its reduced volume and reduced spontaneous curvature, which, in the present case, are $v = 1/\sqrt{2}$ and $m_0 = 0$, respectively, where $1/\sqrt{2}$ is the only reduced volume compatible with a vesicle obtained from the fusion of two spheres of the same radius. As shown in [57], with these parameters, it is possible to reach two axisymmetric configurations with the topology of a sphere, namely one oblate-discocyte shape and one prolate-dumbbell shape. The latter has the lowest energy and, in the present case, is the equilibrium state assigned to the string as the final configuration, $\phi_{\alpha=1}(\boldsymbol{x})$.

Figure 2b shows the free energy profile along the MEP. The free energy of the final configuration (prolate) is $E[\phi_{\alpha=1}]/(8\pi k) \approx 1.12$, which is larger than the initial energy $E[\phi_{\alpha=0}]/(8\pi k) = 1$ of the two spheres. Both values are in excellent agreement with the data reported in [57]. One may notice that the two-spheres configuration possesses a sequence of neutral equilibrium states, corresponding to rigid translations during which the two vesicles approach/separate from each other (configurations i from 1 to 11, as also depicted in Fig. 2a). The saddle point consists of two spheres connected by a small narrow neck and is located between configurations $i = 14$ and $i = 15$, with the latter having the highest energy of the two, $E[\phi_{\alpha=\alpha_c}]/(8\pi k) \approx 1.45$. It should be noticed that such a configuration possesses the bending energy of two spheres together with the Gaussian energy and the topology of a single sphere. Hence, the forward and backward free energy barriers are $\Delta E^{\dagger}_{0\to1}/(8\pi k) \approx 0.45$ and $\Delta E^{\dagger}_{1\to0}/(8\pi k) \approx 0.33$, respectively. Considering a bending rigidity k of order $20\,k_BT$ [11], it turns out that both fusion and fission processes cannot take place spontaneously and require further agents in order to happen, in addition to the elasticity and thermal fluctuations. These agents are typically protein systems. Still, in Fig. 2b, it is possible to observe a substantial asymmetry between fusion and fission, with a much steeper energy increase required to reach the transition state in the fusion process.

The main plots in Fig. 2c provide the bending and Gaussian contributions to the free energy along the MEP. Apparently, the forward barrier $\Delta E^{\dagger}_{0\to1}$ is almost entirely due to the Gaussian energy jump associated with the topological change. On the other hand, the backward barrier $\Delta E^{\dagger}_{1\to0}$ builds up continuously with the progressive deformation of the prolate shape to form the narrow neck preceding the actual fission. The inset shows the evolution of the area and enclosed volume along the MEP, confirming that the constraints are perfectly satisfied at each string image.

The formation of the catenoid-like neck [58] has also been observed in the experiments [27]. Operationally, we define the neck region as the z-chunk of the fused vesicle where the local contribution to the Gaussian energy,

$$E_G^{\mathrm{neck}}(Z) = k_G\,\frac{35}{16\sqrt{2}}\,\epsilon^3\int_{-Z}^{+Z} dz \int 2\pi r\,\psi_G\,dr\,, \qquad (8)$$

is positive. The Gaussian energy of the neck along the MEP is shown in the top panel of Fig. 3, blue line. Proceeding from left to right, $E_G^{\mathrm{neck}}(Z)/(8\pi k)$ sharply increases to a value close to (though smaller than) 0.5 and subsequently decreases. According to the Canham-Helfrich model, the sharp interface Gaussian energy of a sphere is $E_G^{\mathrm{CH}}/(8\pi k) = -0.5$. Given two initially disjoint sharp spheres ($E_G^{\mathrm{CH}}/(8\pi k) = -1$), a joining neck changes the topology and reduces the energy to that of a single sphere, $E_G^{\mathrm{CH}}/(8\pi k) = -0.5$. There are two main reasons why the present free energy provides a neck contribution that is slightly smaller than 0.5: i) close to the transition state, the curvature of the neck generatrix is comparable with the finite thickness of the bilayer, so that the sharp-interface model is inappropriate; ii) the value 0.5

is an upper limit for the sharp interface Gaussian energy of the neck (see, e.g., the Gauss Map in [59]). Evidently, $E_G^{\text{neck}}(Z)$ is the main contribution to the forward barrier $\Delta E^{\dagger}_{0\to 1}/(8\pi k) \approx 0.45$. Proceeding to the right along the MEP, beyond the saddle point, $E_G^{\text{neck}}(Z)$ progressively decreases, top panel of Fig. 3, blue line. Since, Fig. 2c, in that region the total Gaussian energy remains overall constant, $E_G/(8\pi k) = -0.5$, the (Gaussian) energy lost by the neck is redistributed to the remaining, dome-like parts of the vesicle. Figure 3, top panel, orange line with dots, also provides the neck Gaussian energy as a post-processing based on the sharp interface Canham-Helfrich energy, equation 1, computed considering the $\phi = 0$ level set as the membrane midsurface, see the Supplementary Information for additional details.

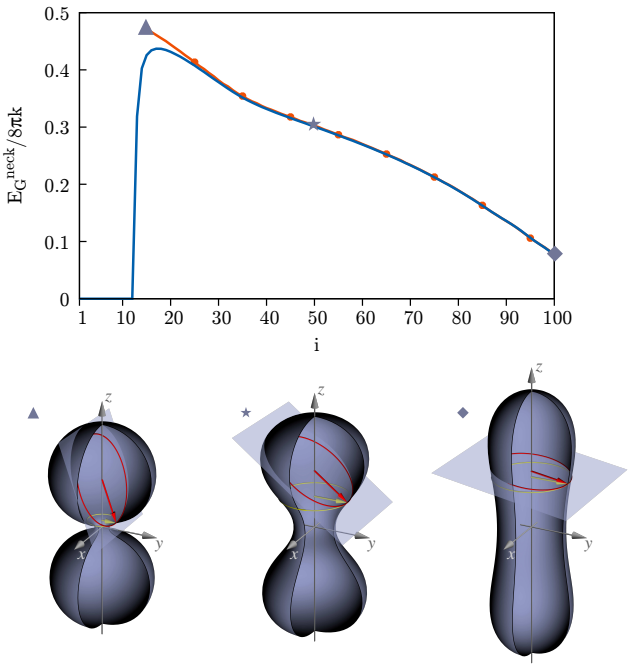

Fig. 3 Neck Gaussian energy. Top panel: normalized Gaussian energy of the neck, $E_G^{\text{neck}}(Z)/(8\pi k)$, equation (8), along the MEP (blue line). The orange line with dots provides the neck Gaussian energy as a post-processing based on the sharp interface Canham-Helfrich energy, equation 1, computed considering the $\phi = 0$ isoline as the membrane midsurface: $E^{\text{neck}}_{G,CH}(Z)/(8\pi k) = \sqrt{1-(r(Z)/R_n)^2}/2$. The agreement between the two curves progressively deteriorates when getting closer to the saddle point, due to the increasing curvature of the membrane generatrix. In this region, the finite thickness of the bilayer plays a crucial role and is taken into account by the phase-field. Bottom panel: three membrane configurations sketching the upper (yellow) circular boundary of the neck with its curvature radius $r(Z)$ (yellow arrow), and the osculating (red) circle to the vesicle cross section with the cutting plane passing through the neck boundary and containing both the surface normal and the tangent to the circle. The radius R_n of the osculating circle is shown as a red arrow. The position of each configuration along the MEP is denoted by the corresponding symbol (triangle, star and rhombus).

Force fields

Figure 4 focuses on the region of the MEP where the most relevant events associated with the topological transition take place, images $i = 11, \ldots, 40$. The contour plots in the lower half panels of Fig. 4 provide the structure of the phase-field as a function of radius r^* and axial coordinate z^*, with ϕ smoothly joining the inner region $\phi = 1$ to the outer region $\phi = -1$ through the layer of dimensionless thickness $\ell^*_{pf} = 6$.

As explained in Section Methods, each image of the string can be rendered a state of equilibrium by introducing a force field $\boldsymbol{f} = -\delta E/\delta\phi\boldsymbol{\nabla}\phi$ that counterbalances the membrane elastic reaction. Considering the forward transition, $0 \to 1$, such force field from $\alpha = 0$ to $\alpha = \alpha_c$ can be interpreted as the external force needed to drive the transition under quasi-static conditions, thus spending the minimal work $\mathcal{W}_{0\to 1} = \Delta E^{\dagger}_{0\to 1}$. Once the critical state is overcome, the system can be left to evolve spontaneously until it reaches the final equilibrium state $\alpha = 1$. Symmetric considerations hold for the backward transition $1 \to 0$. The dimensionless vector fields $\boldsymbol{f}^*_{\alpha}(\boldsymbol{x})$ are depicted as arrows in each panel of Fig. 4, where, for the sake of better readability, they are plotted only on the $\phi = 0$ isoline. The contour plots on the upper part of each panel display the component of the force normal to ϕ-isolines. It should be noticed that the scale of the arrows changes from panel to panel, at least for the upper frames, $i = 11, \ldots, 14$. For the forward process, the latter are the configurations achieved just before the critical state. In this region, the MEP is particularly steep, requiring more intense forces, which result to be strongly localized near the vesicles contact region. On the contrary, the backward process requires a more distributed force field, as shown in images $i = 15, \ldots, 40$. The arrows reverse their direction between configurations $i = 14$ and $i = 15$, showing that in this interval the force field vanishes, confirming that the critical state occurs somewhere between these two images.

Insights into the action of proteins from the MEP

The forces required for overcoming the fusion topological barrier are too strong to be directly exerted by the sole mechanical action of proteins. For example, setting $k = 20\,k_BT$ [11], the resulting activation energy, $\Delta E^{\dagger}_{0\to 1} \approx 226\,k_BT$, is associated with a very steep free energy profile. Consistently with the present findings, Deserno [60] suggests that fusion proteins, besides a mechanical action, may contribute to lowering the energy barrier by locally modifying the Gaussian modulus in the contact region of the approaching membranes. Indeed, the introduction of a suitable, spatially dependent

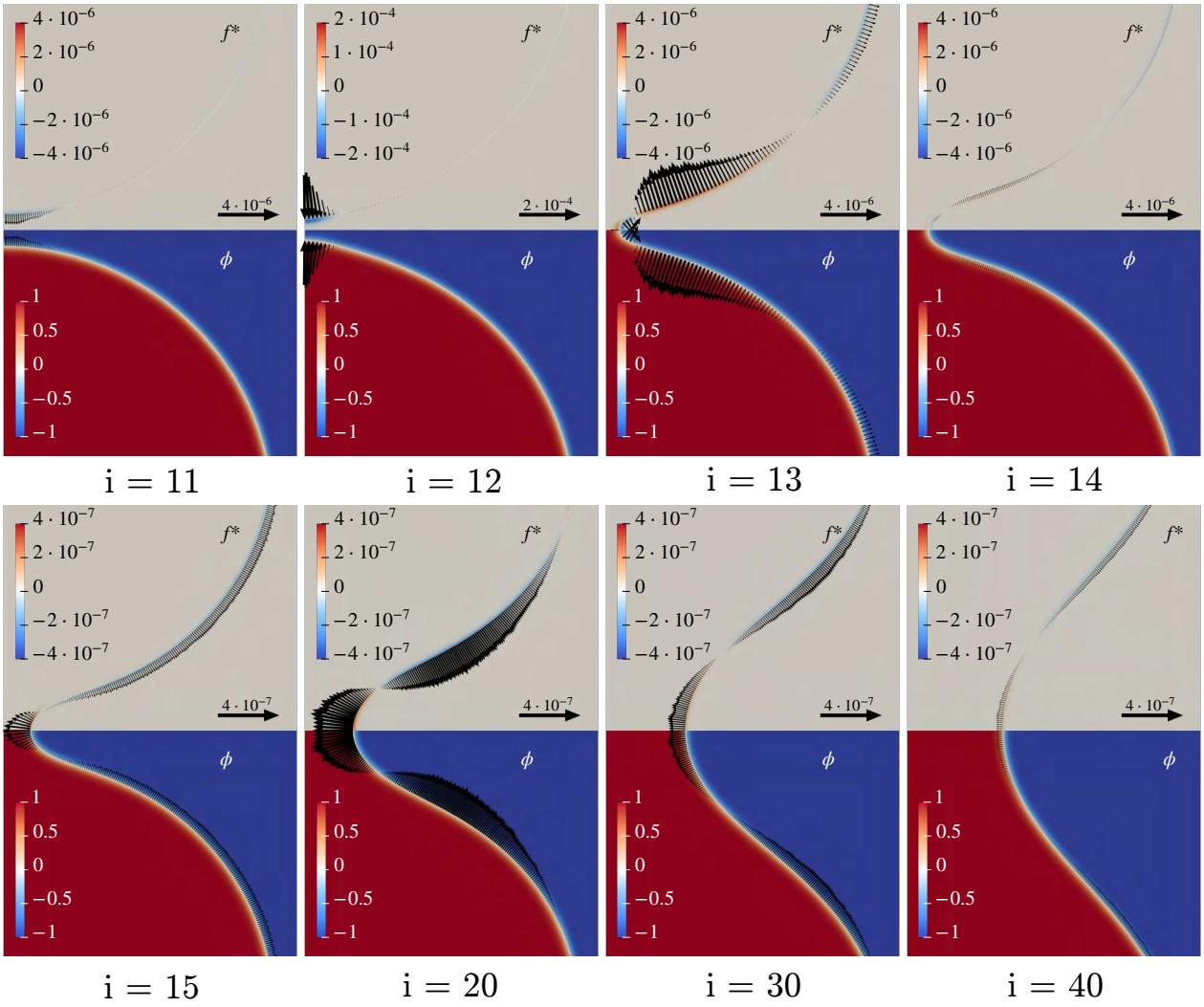

Fig. 4 Force fields along the MEP. Detailed views in the $r^* - z^*$ plane of the vesicle configurations along the MEP. The index $i = (N-1)\alpha_i + 1$ numbers the images on the string. Vectors, plotted for clarity only on the $\phi = 0$ isoline, provide the force field $\boldsymbol{f} = -\delta E/\delta\phi \boldsymbol{\nabla}\phi$ required to keep the vesicle in equilibrium in the given configuration, balancing the internal elastic reaction. The contours in the upper part of each view show the normal component of the force, while those on the lower part depict the field ϕ. For a better visibility, vectors are scaled according to the reference arrow in each plot.

Gaussian modulus is expected to reduce the stiffness associated with the GB theorem, opening alternative routes to the topological change. Our results show that this scenario is actually possible since the forces associated with the Gaussian energy are localized in the region of contact between the two spheres and, therefore, it is reasonable that a variation of k_G in such a region could lower the activation energy. For example, this situation is compatible with the observation that influenza virus hemagglutinin proteins, in addition to having an apposition activity, are also able to perturb the membrane lipid bilayer by insertion of their amphipathic fusion peptide [61]. Interestingly, the present phase-field approach can be easily adapted to the instance of a topological transition with a spatially dependent Gaussian modulus, a case we leave for a future work.

As anticipated, the forces at play during fission are more distributed and less intense than for fusion. The large region they act on, Fig. 4, is consistent with the cooperation of several protein systems, like, e.g., in clathrin mediated endocytosis, which involves clathrins polymerization and the subsequent action of the constrictase dynamin [27]. One can estimate the minimal work the protein system needs to perform to induce the topological change by comparing the free energy barrier $\Delta E^{\dagger}_{1\to 0}$ with the protein work $\mathcal{W}_{1\to 0} = f_p\,\Delta r$, where f_p is the order of magnitude of the protein force and $\Delta r = r_{max} - r_0$ is the change in vesicle radius at the neck, between the equilibrium prolate (r_{max}) and the saddle point configurations (r_0). Given the scale of the system described above, we find $\Delta r = 37.4\,\text{nm}$ which, from the barrier height, provides $f_p = 0.91\,k$ pN$/k_BT$. Interestingly, for the values

of k proper of fluid lipid membranes, we obtain protein forces in fairly good agreement with the experimental estimates reported in [25], e.g. $\simeq 20\,\mathrm{pN}$ for dynamin, $\simeq 65\,\mathrm{pN}$ for ESCRT-III and $\simeq 80\,\mathrm{pN}$ for FtsZ. For example, by assuming $k = 20\,k_BT$, we obtain a protein constriction force f_p of 18.2 pN. For the same bending rigidity, Fig. 5 shows, red curve with squares, the energy needed to complete the fission process as a function of the current neck radius r_n, $\Delta E(r_n) = E(r_n) - E(r_0)$ (note that the fission proceeds from larger to smaller neck radii, i.e. from right to left along the abscissa). The corresponding image number i along the MEP is provided on the second abscissa axis on the top of the frame. The slope of the plot, $d\Delta E/dr_n$, orange line with triangles, provides the estimate of the constriction force (positive when constrictive). A plateau is apparent at $d\Delta E/dr_n \simeq 20\,\mathrm{pN}$ in the range of radii $16 \leq r_n \leq 21\,\mathrm{nm}$. Notably, it is known from the literature [62] that, e.g., dynamin polymerizes on tubules with radius between 10 and 30 nm, exherting forces of the order of 20 pN. In order to facilitate comparison with published data, Fig. 5 also provides in blue, with dots, $f_p = \Delta E(r_n)/(r_n - r_0)$.

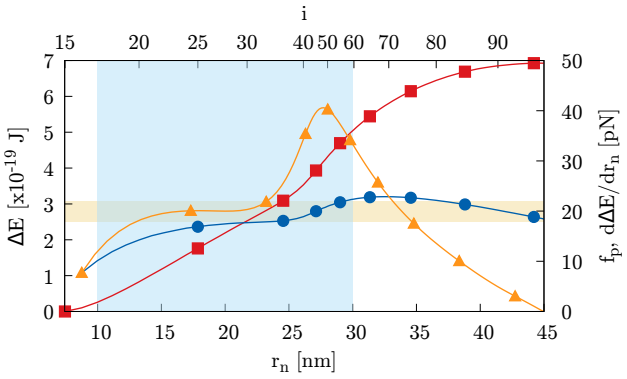

Fig. 5 Proteins and constriction forces. Red curve with squares: energy needed to complete the fission as a function of the current neck radius r_n, $\Delta E = E(r_n) - E(r_0)$ vs r_n. The second abscissa axis on top of the frame provides the image number i along the MEP. Orange curve with triangles: estimated constriction force (second ordinate axis on the right), $d\Delta E/dr_n$ vs r_n. Blue curve with dots: $f_p = \Delta E(r_n)/(r_n - r_0)$ vs r_n. The vertical light blue band represents the range in which dynamin polymerizes [62]. The horizontal light orange strip depicts the value of dynamin constriction force measured in experiments [25, 62].

DISCUSSION

We have provided an unprecedented description of the full-scale process of topology change in the fusion/fission process of two large unilamellar vesicles (LUVs) with an approach that can be extended to deal with giant unilamellar vesicles (GUVs). The proposed free energy accounts for the Canham-Helfrich Gaussian energy jumps as prescribed by the GB theorem, and, far from the topological changes, recovers the Canham-Helfrich Hamiltonian itself in the limit of small bilayer thickness. However, during topological transitions, when the relative distance between approaching membrane segments becomes comparable to the bilayer thickness, the scale invariance of the asymptotic Canham-Helfrich Hamiltonian is broken. For such a reason, we defined the scale of our system by matching the lipid bilayer thickness with the diffuse interface width. From a mathematical standpoint, our proposal should be interpreted as a rational way to regularize the singularity, leading to a process that smoothly matches the external solution before and after the transition, allowing the description of the whole process. The free energy clearly misses the many molecular details associated with the dynamics of the lipids forming the bilayer. However, the correction due to such details is small as compared to the energy barrier associated with the full-scale evolution of the vesicle.

Naively, one may argue that proteins systems could have evolved in Nature to overcome the large barrier that stabilizes the vesicle topology by following a minimal energy pathway. Hence, by means of the new free energy functional, we have evaluated the minimal free energy path for the transition and extracted the force field able to drive the process with minimal work expenditure. The free energy profile we find show the strong asymmetry between the fusion and the fission processes. For fusion, the required force field is extremely intense and suggests that proteins could locally modify the Gaussian modulus during the topological change, a case that can finally be addressed with the presented approach. On the contrary, as regards fission, the obtained spatial scales and forces are consistent with the experimental estimates for typical fission protein systems, like the ESCRT-III, FtsZ, and dynamin.

Finally, it can be noted that the proposed approach can naturally be coupled with hydrodynamics [63, 64] to include the dynamics of external and internal aqueous environments. One may also stress that the Gaussian energy functional can find a much broader scope, e.g., as an indicator of the topological genus in the context of cluster analysis [65, 66], or as a way to provide a barrier towards undesired/unphysical fusion processes. A compelling example concerns emulsions where surfactant-covered droplets behave much like lipid micelles [67, 68], suggesting that the Gaussian energy could play a role in the emulsification process.

METHODS

Sharp interface limit

An energy $E[\phi]$, equation (3), is associated with each field configuration and is such as to admit local minimizers of the form

$$\phi(\boldsymbol{x}) = f\left(\frac{d(\boldsymbol{x})}{\epsilon}\right), \tag{9}$$

where $d(\cdot)$ is the signed distance function from the membrane midsurface Γ. We choose to define the signed distance such that $\boldsymbol{n} = \boldsymbol{\nabla} d$ computed on Γ is equal to the inward-pointing unit normal to the vesicle. Setting $d^*(\boldsymbol{x}) = d(\boldsymbol{x})/\epsilon$, we also require that $\lim_{d^*\to\pm\infty}\phi = \pm 1$ and $\phi = 0$ for $d = 0$. Therefore, ± 1 are the values for the stable phases of the inside and outside bulk and the level set $\phi = 0$ identifies the membrane midsurface. Physically, the free energy functional should recover the Canham-Helfrich Hamiltonian, equation (1), in the limit of small width-to-vesicle-extension ratio. $E_B[\phi]$ was already introduced in [34] to model the bending energy of the membrane, while $E_G[\phi]$ is the new term proposed here to account for the Gaussian energy.

As anticipated, our purpose here is to show that, under the general ansatz (9) and in the sharp-interface limit ($\epsilon/D_{ve} = \lambda << 1$), minimizing the phase-field free energy functional (3) is equivalent to minimizing the Canham-Helfrich free energy. Denoting with a prime the derivative done with respect to $d^*(\boldsymbol{x})$, a direct computation leads to

$$E_B[\phi] = k\,\frac{3}{4\sqrt{2}}\,\lambda\int_{\bar\Omega}\left[\frac{1}{\lambda^2}\Big(f'' - (f^2-1)f\Big) + \right. \\ \left. +\ \frac{1}{\lambda}\Big(f'\,\bar{\boldsymbol{\nabla}}\cdot\boldsymbol{n} + (1-f^2)\sqrt{2}\bar m\Big)\right]^2 d\bar V, \tag{10}$$

$$E_G[\phi] = k_G\,\frac{35}{16\sqrt{2}}\int_{\bar\Omega}\frac{f'^4}{\lambda}\Big[(\bar{\boldsymbol{\nabla}}\cdot\boldsymbol{n})^2 + \boldsymbol{n}\cdot\bar{\boldsymbol{\nabla}}(\bar{\boldsymbol{\nabla}}\cdot\boldsymbol{n})\Big]\,d\bar V, \tag{11}$$

where we have denoted with a bar the dimensionless lengths obtained by dividing by D_{ve}. Therefore, in order to minimize $E = E_B + E_G$, as $\lambda\to 0$, the leading-order term f_0 of $\phi(\boldsymbol{x}) = f(d^*(\boldsymbol{x})) = f_0(d^*(\boldsymbol{x})) + \sum_{i=1}^{+\infty}\lambda^i f_i(d^*(\boldsymbol{x}))$ must satisfy $f_0'' = (f_0^2-1)f_0$, which has the solution

$$f_0(d^*(\boldsymbol{x})) = \tanh\left(\frac{d(\boldsymbol{x})}{\epsilon\sqrt{2}}\right). \tag{12}$$

Hence, ϵ is actually related to the width of the interface. Moreover, by repeating the computations done in [69] for the bending energy alone, it is possible to show that, also in the presence of the new Gaussian energy term, one finds $f_1(d^*(\boldsymbol{x})) \equiv 0$ (see the Supplementary Information for the whole computation). Therefore, given that $\sqrt{2}f_0' = (1-f_0^2)$, we are left with

$$E_B[\phi] = k\frac{3}{4\sqrt{2}}\int_{\bar\Omega}\frac{f_0'^2}{\lambda}(\bar{\boldsymbol{\nabla}}\cdot\boldsymbol{n} + 2\bar m)^2\,d\bar V\ +\ O(\lambda), \tag{13}$$

$$E_G[\phi] = \\ k_G\frac{35}{16\sqrt{2}}\int_{\bar\Omega}\frac{f_0'^4}{\lambda}\Big[(\bar{\boldsymbol{\nabla}}\cdot\boldsymbol{n})^2 + \boldsymbol{n}\cdot\bar{\boldsymbol{\nabla}}(\bar{\boldsymbol{\nabla}}\cdot\boldsymbol{n})\Big]d\bar V\ +\ O(\lambda^2). \tag{14}$$

Denoting with k_1 and k_2 the principal curvatures, we have $\boldsymbol{\nabla}\cdot\boldsymbol{n} = -(k_1+k_2) = -2M$ and $\boldsymbol{n}\cdot\boldsymbol{\nabla}k_i = k_i^2$, with the result that $(\boldsymbol{\nabla}\cdot\boldsymbol{n})^2 + \boldsymbol{n}\cdot\boldsymbol{\nabla}(\boldsymbol{\nabla}\cdot\boldsymbol{n}) = 2k_1k_2 = 2G$. Now, noticing that for $\lambda\to 0$ one finds $f_0'^2(\bar d(\boldsymbol{x})/\lambda)/\lambda \xrightarrow{\mathcal{W}}\ 2\sqrt{2}/3\ \delta(\bar d(\boldsymbol{x}))$, $f_0'^4(\bar d(\boldsymbol{x})/\lambda)/\lambda \xrightarrow{\mathcal{W}}\ 8\sqrt{2}/35\ \delta(\bar d(\boldsymbol{x}))$, where $\delta(x)$ is the Dirac delta function and $\mathcal{W}$ denotes a weak limit in the sense of distributions, and getting back to dimensional variables, the asymptotic behavior follows as

$$E[\phi]\ \sim\ 2k\int_\Gamma (M-m)^2\,dS\ +\ k_G\int_\Gamma G\,dS, \tag{15}$$

i.e., the phase-field energy functional reproduces the Canham-Helfrich free energy in the sharp-interface limit ($\epsilon/D_{ve} << 1$). It is worth noticing that the inclusion of the Gaussian energy, which is subdominant in λ, preserves the hyperbolic tangent form (12) of the leading order solution together with $f_1(d^*(\boldsymbol{x})) \equiv 0$, as for the more standard model with the bending energy alone [34]. Since $f_1(d^*(\boldsymbol{x})) \equiv 0$, the desired expression of the bending energy is retained at order λ^{-1}, and the accuracies $O(\lambda)$ and $O(\lambda^2)$ are guaranteed in Eqs. (13), (14), respectively. Furthermore, in our formulation, the phase-field Gaussian energy (6) has no singularities and actually depends at most on derivatives of order two, as it is possible to see by replacing $\boldsymbol{\nabla}\phi\cdot\boldsymbol{\nabla}\nabla^2\phi$ with $\nabla^2|\boldsymbol{\nabla}\phi|^2/2 - \mathbf{H}_\phi : \mathbf{H}_\phi$ in (7), where $\mathbf{H}_\phi$ is the Hessian matrix of the field. As regards the incompressibility of the membrane, we impose the geometrical constraints described in Section Results using the functionals

$$A[\phi] = \frac{3}{4\sqrt{2}}\,\epsilon\int_\Omega\left[\frac{(1-\phi^2)^2}{2\epsilon^2}\ +\ |\boldsymbol{\nabla}\phi|^2\right]dV, \tag{16}$$

$$V[\phi] = \int_\Omega\frac{(1+\phi)}{2}\,dV, \tag{17}$$

which respectively behave like the vesicle area and enclosed volume in the sharp interface limit.

Gauss-Bonnet theorem

Let's assume that

$$\phi(\boldsymbol{x}) = \tanh\left(\frac{d(\boldsymbol{x})}{\epsilon\sqrt{2}}\right), \tag{18}$$

where $\boldsymbol{x}\in\Omega$, being Ω a cylindrical domain of radius R and height L in the ordinary three-dimensional space, and $d(\cdot)$ the signed distance from an axisymmetric surface in Ω. This assumption leads to $|\boldsymbol{\nabla}\phi| = (1-\phi^2)/(\epsilon\sqrt{2})$, and, moreover, we set $h(\phi) = \left[(1-\phi^2)/(\epsilon\sqrt{2})\right]^4$. Using the cylindrical coordinates system, it is possible to show by a direct computation [46] that one of the two principal curvatures is $k_1 = -\partial_r\phi/(r|\boldsymbol{\nabla}\phi|)$. Therefore, remembering that $\boldsymbol{\nabla}\cdot\boldsymbol{n} = -(k_1+k_2)$ and $\boldsymbol{n}\cdot\boldsymbol{\nabla}k_i = k_i^2$, with $\boldsymbol{n} = \boldsymbol{\nabla}d$, equation (14) can be rewritten as

$$\begin{aligned}
&E_G[\phi]\ = \\
&=\ k_G\frac{35}{8\sqrt{2}}\epsilon^3\int_\Omega h(\phi)\,k_1k_2\,dV\ = \\
&=\ -k_G\frac{35}{8\sqrt{2}}\epsilon^3\int_\Omega h(\phi)\,\boldsymbol{\nabla}\cdot(\boldsymbol{n}\,k_1)\,dV\ = \\
&=\ k_G\frac{35}{8\sqrt{2}}\epsilon^3\int_\Omega\frac{dh}{d\phi}\,\boldsymbol{\nabla}\phi\cdot\boldsymbol{n}\,k_1\,dV\ +\ I_{\partial\Omega}\ = \\
&=\ k_G\frac{35}{8\sqrt{2}}\epsilon^3\int_\Omega\frac{dh}{d\phi}\,|\boldsymbol{\nabla}\phi|\,k_1\,dV\ +\ I_{\partial\Omega}\ = \\
&=\ -k_G\frac{35}{4\sqrt{2}}\epsilon^3\pi\int_{-L/2}^{+L/2}dz\int_0^R\frac{dh}{d\phi}\,\frac{\partial\phi}{\partial r}\,dr\ +\ I_{\partial\Omega}\ = \\
&= k_G\frac{35}{4\sqrt{2}}\epsilon^3\pi\int_{-L/2}^{+L/2}[h(\phi(r=0,z)) - h(\phi(r=R,z))]dz + \\
&\quad + I_{\partial\Omega}\ ,
\end{aligned}$$

where

$$I_{\partial\Omega} = -\,k_G\frac{35}{8\sqrt{2}}\epsilon^3\int_{\partial\Omega}h(\phi)\,k_1\,\boldsymbol{n}_\Omega\cdot\boldsymbol{n}\,dS\ .$$

Supposing to have a single, connected, closed surface, after letting Ω invade $\mathbb{R}^3$, and considering relation $f_0'^4(\bar{d}(\boldsymbol{x})/\lambda)/\lambda \xrightarrow{\mathcal{W}} 8\sqrt{2}/35\ \delta(\bar{d}(\boldsymbol{x}))$ applied to $h(\phi)$, we obtain

$$\begin{aligned}\lim_{\epsilon\to 0} E_G[\phi] \ &= \\ &= \ 2\pi k_G \int_{-\infty}^{+\infty} \delta(d(r=0,z))\, dz \ = \\ &= \ 4\pi k_G\,(1-g)\ ,\end{aligned}$$

recovering the Gauss-Bonnet theorem, equation (2), in the axially-symmetric case. The last equality is justified by the fact that the Dirac delta function counts the intersections of the surface with the z-axis, which is equivalent to checking whether the surface has a hole.

Numerical scheme

The numerics relies on FFT-based spectral differentiation in cell-centered grids which provide high accuracy solutions, with special regard to the estimate of the Gaussian energy. The accuracy in evaluating the Gaussian energy, equation (6), is shown in Table 1 for a sphere, a torus and a straight cylinder. Given the axial-symmetry of these shapes, all the computations are done in a $[0,40]\times[0,40]$ computational domain in the r^*-z^* plane with a grid of 80×80 nodes. In evaluating the functional, we set $\phi(\boldsymbol{x^*}) = \tanh((\sqrt{r^{*2}+(z^*-20)^2}-10)/\sqrt{2})$ for the sphere, $\phi(\boldsymbol{x^*}) = \tanh((\sqrt{(r^*-20)^2+(z^*-20)^2}-10)/\sqrt{2})$ for the torus and $\phi(\boldsymbol{x^*}) = \tanh((r^*-10)/\sqrt{2})$ for the cylinder, which are obtained imposing equation (12).

Table 1 Gaussian energy computed values, $k_G = -k$.

Shape	$E_G/8\pi k$ (exact)	$E_G/8\pi k$ (numerical)
Sphere	$-5.\cdot 10^{-1}$	$-5.000525\cdot 10^{-1}$
Torus	0.	$-1.729446\cdot 10^{-18}$
Cylinder	0.	$-9.860761\cdot 10^{-32}$

The energy pathways of Section Results are obtained by means of the string method, which is briefly described below. The remaining simulations reported in this paper, i.e. the one shown in Fig. 1 and those in the Supplementary Information, are carried out using the Allen-Cahn dynamics

$$\frac{\partial\phi}{\partial t} = -M\frac{\delta\bar{E}}{\delta\phi}, \tag{19}$$

where M is the mobility coefficient and $\delta\bar{E}/\delta\phi$ is the functional derivative of the augmented energy

$$\begin{aligned}\bar{E}[\phi] &= E[\phi] + \\ &+ \gamma(A[\phi]-A_0) + \frac{1}{2}M_1(A[\phi]-A_0)^2 + \\ &+ \Delta p(V[\phi]-V_0) + \frac{1}{2}M_2(V[\phi]-V_0)^2\ .\end{aligned} \tag{20}$$

Here, the additional terms added to the energy (3) are needed when constraining to A_0 and V_0 the vesicle area (16) and volume (17), respectively. M_1, M_2 are two penalty constants, whereas γ and Δp are updated at each time step according to the *augmented Lagrangian method*, [70]:

$$\gamma^{n+1} \ = \ \gamma^n + M_1(A[\phi^{n+1}]-A_0), \tag{21}$$

$$\Delta p^{n+1} = \ \Delta p^n + M_2(V[\phi^{n+1}]-V_0). \tag{22}$$

Therefore γ and Δp are estimates of the Lagrange multipliers that improve at every time step. Starting from an assigned initial condition, the Allen-Cahn dynamics causes the energy to monotonically decrease in time until it reaches a critical steady-state. The dimensionless time and mobility are $t^* = t/\tau_R$ and $M^* = 8\pi k M\tau_R/\epsilon^3$, respectively, with τ_R a suitable time scale.

With the help of the PETSc library [71], a Crank-Nicolson time-stepping scheme is employed to integrate the Allen-Cahn gradient flow, while a semi-implicit Euler single step scheme is used to solve the more computationally demanding string dynamics. The explicit form of the functional derivative $\delta\bar{E}/\delta\phi$ is given in the Supplementary Information together with some numerical experiments carried out to validate the approach.

String method

The zero-temperature string method [47] is a technique for computing free energy barriers and transition pathways on a given energy landscape. The method proceeds by evolving in time a *string*, namely a curve parameterized by $\alpha\in[0,1]$. For each α the image of the string is a phase-field function $\phi_\alpha(\boldsymbol{x})$ representing a membrane state.

Given an initial guess for the pathway connecting two local minima, the string evolves in time following the dynamics

$$\frac{\partial\phi_\alpha}{\partial t} = -M\left(\frac{\delta\bar{E}}{\delta\phi_\alpha}\right)^{\perp}\ \ \forall\alpha\in[0,1], \tag{23}$$

where M is a mobility coefficient, $\delta\bar{E}/\delta\phi_\alpha$ is the functional derivative of (20) evaluated on the image ϕ_α and $(\delta\bar{E}/\delta\phi_\alpha)^\perp$ is its component normal to the string. This last quantity can be computed as $(\delta\bar{E}/\delta\phi_\alpha)^\perp = \delta\bar{E}/\delta\phi_\alpha - \left\langle\delta\bar{E}/\delta\phi_\alpha\,\middle|\,\tau\right\rangle\tau$, where $\tau = \partial_\alpha\phi_\alpha/\left\langle\partial_\alpha\phi_\alpha\,|\,\partial_\alpha\phi_\alpha\right\rangle^{1/2}$ is the unit tangent to the string and $\langle\cdot\,|\,\cdot\rangle$ is the standard L_2 inner product. In this way, at steady state, the string converges to a minimal energy path [54]. In order to eliminate the trouble of projecting the functional derivative and in order to use the equal arc-length parameterization, the string dynamics can be rewritten [56] as

$$\frac{\partial\phi_\alpha}{\partial t} = -M\frac{\delta\bar{E}}{\delta\phi_\alpha} + \bar{\lambda}\tau\ \ \forall\alpha\in[0,1], \tag{24}$$

where $\bar{\lambda} = \lambda + M\left\langle\delta\bar{E}/\delta\phi_\alpha\,\middle|\,\tau\right\rangle$ and λ is a Lagrange multiplier for the purpose of enforcing the chosen parameterization $\partial_\alpha\left\langle\partial_\alpha\phi_\alpha\,|\,\partial_\alpha\phi_\alpha\right\rangle^{1/2} = 0$.

The algorithm follows the steps:

1. Evolution from t to $t+\Delta t$ of the discrete string, made up of N images ϕ_i, with the dynamics

$$\frac{\partial\phi_i}{\partial t} = -M\frac{\delta\bar{E}}{\delta\phi_i},\ \ i=1,\dots,N\,.$$

Time integration is performed in wave number space by means of the semi-implicit Euler single step scheme. The evolved images at time $t+\Delta t$ are denoted as $\tilde{\phi}_i$.

2. Computation of the arc lengths corresponding to the evolved images:

$$s_0 = 0,$$
$$s_i = s_{i-1} + \left\langle \tilde{\phi}_i - \tilde{\phi}_{i-1} \,\middle|\, \tilde{\phi}_i - \tilde{\phi}_{i-1} \right\rangle^{1/2},$$
$$i = 1, \dots, N\,.$$

   Thus, the evolved images have parameters $\alpha_i = s_i/s_N$.

3. Linear interpolation of the evolved images in order to compute the new images at equal arcs $\alpha_i = i/N$. These are the actual solutions at time $t+\Delta t$. It is worth noticing that linear interpolation conserves vesicles volume.

4. Go back to one and iterate until convergence.

Force fields computation

Given a membrane state, it is possible to compute the external force needed to balance the elastic force arising from the energy of the membrane. For this purpose, let's consider an arbitrary and infinitesimal variation $\delta\phi$ of the phase-field, consistent with the area and volume constraints, if present. This variation results in a spatial displacement $\delta\boldsymbol{x}$ of the field lines. The displacement can be thought to occur in a virtual time interval δt, within which the field lines move with a virtual velocity $\boldsymbol{u}$ such that $\partial\phi/\partial t = -\boldsymbol{\nabla}\phi\cdot\boldsymbol{u}$ (null material derivative condition). By integrating in time this last equation from t to $t+\delta t$, we are left with the first order approximation

$$\delta\phi = -\boldsymbol{\nabla}\phi\cdot\boldsymbol{u}\delta t = -\boldsymbol{\nabla}\phi\cdot\delta\boldsymbol{x}. \tag{25}$$

Hence, the work performed by the external force field $\boldsymbol{f}$ to deform the membrane is

$$\begin{aligned}&\int_\Omega \boldsymbol{f}\cdot\delta\boldsymbol{x}\,dV = \delta\bar{E} = \\ &\int_\Omega \frac{\delta\bar{E}}{\delta\phi}\,\delta\phi\,dV = -\int_\Omega \frac{\delta\bar{E}}{\delta\phi}\boldsymbol{\nabla}\phi\cdot\delta\boldsymbol{x}\,dV,\end{aligned} \tag{26}$$

and one can identify the force field

$$\boldsymbol{f} = -\frac{\delta\bar{E}}{\delta\phi}\boldsymbol{\nabla}\phi\,, \tag{27}$$

thanks to the arbitrariness of $\delta\boldsymbol{x}$.

AUTHOR CONTRIBUTIONS

ACKNOWLEDGMENTS

Support is acknowledged from the 2020 Sapienza Large Project: Dynamics of Biological and Artificial Lipid Bilayer Membranes. Concerning computational resources we acknowledge: PRACE for awarding us access to Marconi successor at CINECA, Italy, PRACE 23rd call project Nr. 2021240074; DECI 17 SOLID project for resource Navigator based in Portugal at `https://www.uc.pt/lca/` from the PRACE aisbl; CINECA award under the ISCRA initiative, for the availability of high performance computing resources and support (ISCRA-B FHDAS).

[1] Pierre C Hohenberg and Bertrand I Halperin, "Theory of dynamic critical phenomena," Reviews of Modern Physics **49**, 435 (1977).

[2] Chelsea T. Barrett and Rebecca Ellis Dutch, "Viral membrane fusion and the transmembrane domain," Viruses **12** (2020).

[3] Stephen C. Harrison, "Viral membrane fusion," Nature Structural & Molecular Biology **15**, 690 – 698 (2008).

[4] Jeremy G. Carlton, Hannah S Jones, and Ulrike S. Eggert, "Membrane and organelle dynamics during cell division," Nature Reviews Molecular Cell Biology **21**, 151–166 (2020).

[5] Leonid V. Chernomordik and Michael M. Kozlov, "Protein-lipid interplay in fusion and fission of biological membranes." Annual review of biochemistry **72**, 175–207 (2003).

[6] Rumiana Tenchov, Robert Bird, Allison Curtze, and Qiongqiong Zhou, "Lipid nanoparticles-from liposomes to mrna vaccine delivery, a landscape of research diversity and advancement." ACS nano (2021).

[7] Xucheng Hou, Tal Z. Zaks, Robert Langer, and Yizhou Dong, "Lipid nanoparticles for mrna delivery," Nature Reviews. Materials , 1 – 17 (2021).

[8] Michael J. Mitchell, Margaret M. Billingsley, Rebecca M Haley, Marissa E. Wechsler, Nicholas A. Peppas, and Robert S Langer, "Engineering precision nanoparticles for drug delivery," Nature Reviews. Drug Discovery , 1 – 24 (2020).

[9] Peter B. Canham, "The minimum energy of bending as a possible explanation of the biconcave shape of the human red blood cell." Journal of theoretical biology **26 1**, 61–81 (1970).

[10] Wolfgang. Helfrich, "Elastic properties of lipid bilayers: Theory and possible experiments," Zeitschrift für Naturforschung C **28**, 693 – 703 (1973).

[11] Rumiana Dimova, "Recent developments in the field of bending rigidity measurements on membranes." Advances in colloid and interface science **208**, 225–34 (2014).

[12] Markus Deserno, "Fluid lipid membranes: From differential geometry to curvature stresses," Chemistry and Physics of Lipids **185**, 11–45 (2015).

[13] Søren Lorenzen, Rolf-M. Servuss, and Wolfgang. Helfrich, "Elastic torques about membrane edges: A study of pierced egg lecithin vesicles." Biophysical journal **50 4**, 565–72 (1986).

[14] A. I. Derzhanski, Alexander G. Petrov, and M. D. Mitov, "Molecular asymmetry and saddle-splay elasticity in lipid bilayers," Annales De Physique **3**, 297–297 (1978).

[15] Mingyang Hu, John J Briguglio, and Markus Deserno, "Determining the gaussian curvature modulus of lipid membranes in simulations." Biophysical journal **102 6**, 1403–10 (2012).

[16] Rumiana Dimova and Carlos Manuel Marques, "The giant vesicle book," (2019).

[17] Rikhia Ghosh, Vahid Satarifard, Andrea Grafmüller, and Reinhard Lipowsky, "Budding and fission of nanovesicles induced by membrane adsorption of small solutes," ACS Nano **15**, 7237 – 7248 (2021).

[18] Nga T. Ho, Marc Siggel, Karen V Camacho, Ramachandra M. Bhaskara, Jacqueline M Hicks, Yun-Chiao Yao, Yuliang Zhang, Jürgen Köfinger, Gerhard Hummer, and Aleksandr Noy, "Membrane fusion and drug delivery with carbon nanotube porins," Proceedings of the National Academy of Sciences of the United States of America **118** (2021).

[19] Siewert J. Marrink and Alan E. Mark, "The mechanism of vesicle fusion as revealed by molecular dynamics simulations." Journal of the American Chemical Society **125 37**, 11144–5 (2003).

[20] Volker Knecht and Siewert J. Marrink, "Molecular dynamics simulations of lipid vesicle fusion in atomic detail." Biophysical journal **92 12**, 4254–61 (2007).

[21] Julian C. Shillcock and Reinhard Lipowsky, "Tension-induced fusion of bilayer membranes and vesicles," Nature Materials **4**, 225–228 (2005).

[22] Andrea Grafmüller, Julian C. Shillcock, and Reinhard Lipowsky, "Pathway of membrane fusion with two tension-dependent energy barriers." Physical review letters **98 21**, 218101 (2007).

[23] Y G Smirnova, Herre Jelger Risselada, and Marcus Müller, "Thermodynamically reversible paths of the first fusion intermediate reveal an important role for membrane anchors of fusion proteins," Proceedings of the National Academy of Sciences **116**, 2571 – 2576 (2019).

[24] Y G Smirnova, Marc Fuhrmans, Israel A Barragan Vidal, and Marcus Müller, "Free-energy calculation methods for collective phenomena in membranes," Journal of Physics D **48**, 343001 (2015).

[25] Jan Steinkühler, Roland L. Knorr, Ziliang Zhao, Tripta Bhatia, Solveig Mareike Bartelt, Seraphine Valeska Wegner, Rumiana Dimova, and Reinhard Lipowsky, "Controlled division of cell-sized vesicles by low densities of membrane-bound proteins," Nature Communications **11** (2020).

[26] Hans-Günther Döbereiner, Josef Alfons Käs, D. A. Noppl, Irene Sprenger, and Erich. Sackmann, "Budding and fission of vesicles." Biophysical journal **65 4**, 1396–403 (1993).

[27] Ori Avinoam, Martin Schorb, Carsten Jörn Beese, John A. G. Briggs, and Marko Kaksonen, "Endocytic sites mature by continuous bending and remodeling of the clathrin coat," Science **348**, 1369 – 1372 (2015).

[28] Guohua Lei and Robert C. Macdonald, "Lipid bilayer vesicle fusion: intermediates captured by high-speed microfluorescence spectroscopy." Biophysical journal **85 3**, 1585–99 (2003).

[29] Marina Fix, Thomas J. Melia, Jyoti K. Jaiswal, Joshua Z. Rappoport, Daoqi You, Thomas H. Söllner, James E. Rothman, and Sanford M. Simon, "Imaging single membrane fusion events mediated by snare proteins." Proceedings of the National Academy of Sciences of the United States of America **101 19**, 7311–6 (2004).

[30] Christopher K. Haluska, Karin A. Riske, Valerie Marchi-Artzner, Jean-Marie Lehn, Reinhard Lipowsky, and Rumiana Dimova, "Time scales of membrane fusion revealed by direct imaging of vesicle fusion with high temporal resolution," Proceedings of the National Academy of Sciences **103**, 15841 – 15846 (2006).

[31] Sebastian Aeffner, Tobias Reusch, Britta Weinhausen, and Tim Salditt, "Energetics of stalk intermediates in membrane fusion are controlled by lipid composition," Proceedings of the National Academy of Sciences **109**, E1609 – E1618 (2012).

[32] J G Lee and Barry R. Lentz, "Secretory and viral fusion may share mechanistic events with fusion between curved lipid bilayers." Proceedings of the National Academy of Sciences of the United States of America **95 16**, 9274–9 (1998).

[33] Claire François-Martin, James E. Rothman, and Frederic Pincet, "Low energy cost for optimal speed and control of membrane fusion," Proceedings of the National Academy of Sciences **114**, 1238 – 1241 (2017).

[34] Qiang Du, Chun Liu, and Xiaoqiang Wang, "A phase field approach in the numerical study of the elastic bending energy for vesicle membranes," Journal of Computational Physics **198**, 450–468 (2004).

[35] Qiang Du, Chun Liu, Rolf J. Ryham, and Xiaoqiang Wang, "Modeling the spontaneous curvature effects in static cell membrane deformations by a phase field formulation," Communications on Pure and Applied Analysis **4**, 537–548 (2005).

[36] Qiang Du, Chun Liu, and Xiaoqiang Wang, "Simulating the deformation of vesicle membranes under elastic bending energy in three dimensions," J. Comput. Phys. **212**, 757–777 (2006).

[37] Felix Campelo and Aurora Hernández-Machado, "Dynamic model and stationary shapes of fluid vesicles," The European Physical Journal E **20**, 37–45 (2006).

[38] Rui Gu, Xiaoqiang Wang, and Max D. Gunzburger, "Simulating vesicle-substrate adhesion using two phase field functions," J. Comput. Phys. **275**, 626–641 (2014).

[39] Rui Gu, Xiaoqiang Wang, and Max D. Gunzburger, "A two phase field model for tracking vesicle–vesicle adhesion," Journal of Mathematical Biology **73**, 1293–1319 (2016).

[40] Xiaoqiang Wang and Qiang Du, "Modelling and simulations of multi-component lipid membranes and open membranes via diffuse interface approaches," Journal of Mathematical Biology **56**, 347–371 (2008).

[41] Felix Campelo and Aurora Hernández-Machado, "Model for curvature-driven pearling instability in membranes." Physical review letters **99 8**, 088101 (2007).

[42] Guillermo Lázaro, Aurora Hernández-Machado, and Ignacio Pagonabarraga, "Rheology of red blood cells under flow in highly confined microchannels: I. effect of elasticity." Soft matter **10 37**, 7195–206 (2014).

[43] Guillermo Lázaro, Aurora Hernández-Machado, and Ignacio Pagonabarraga, "Collective behavior of red blood cells in confined channels," The European Physical Journal E **42**, 1–9 (2019).

[44] Rafael A. Barrio, Tomas Alarcon, and Aurora Hernández-Machado, "The dynamics of shapes of vesicle membranes with time dependent spontaneous curvature,"

PLoS ONE **15** (2020).
[45] Guillermo Lázaro, Ignacio Pagonabarraga, and Aurora Hernández-Machado, "Phase-field theories for mathematical modeling of biological membranes." Chemistry and physics of lipids **185**, 46–60 (2015).
[46] Qiang Du, Chun Liu, and Xiaoqiang Wang, "Retrieving topological information for phase field models," SIAM J. Appl. Math. **65**, 1913–1932 (2005).
[47] E Weinan, Weiqing Ren, and Eric Vanden-Eijnden, "String method for the study of rare events," Physical Review B **66**, 052301 (2002).
[48] Weiqing Ren, "Wetting transition on patterned surfaces: transition states and energy barriers," Langmuir **30**, 2879–2885 (2014).
[49] James F Lutsko, "How crystals form: A theory of nucleation pathways," Science advances **5**, eaav7399 (2019).
[50] Mirko Gallo, Francesco Magaletti, Davide Cocco, and Carlo Massimo Casciola, "Nucleation and growth dynamics of vapour bubbles," Journal of Fluid Mechanics **883** (2020).
[51] Francesco Magaletti, Mirko Gallo, and Carlo Massimo Casciola, "Water cavitation from ambient to high temperatures," Scientific reports **11**, 1–10 (2021).
[52] Achim Guckenberger and Stephan Gekle, "Theory and algorithms to compute helfrich bending forces: a review." Journal of physics. Condensed matter : an Institute of Physics journal **29 20**, 203001 (2017).
[53] Mara Denisse Rueda-Contreras, Andreu F Gallen, J Roberto Romero-Arias, Aurora Hernandez-Machado, and Rafael A Barrio, "On gaussian curvature and membrane fission," Scientific Reports **11**, 1–10 (2021).
[54] Maria K. Cameron, Robert V. Kohn, and Eric Vanden-Eijnden, "The string method as a dynamical system," Journal of Nonlinear Science **21**, 193–230 (2011).
[55] Luca Maragliano, Alexander Fischer, Eric Vanden-Eijnden, and Giovanni Ciccotti, "String method in collective variables: Minimum free energy paths and isocommittor surfaces," The Journal of chemical physics **125**, 024106 (2006).
[56] Weinan E, Weiqing Ren, and Eric Vanden-Eijnden, "Simplified and improved string method for computing the minimum energy paths in barrier-crossing events." The Journal of chemical physics **126 16**, 164103 (2007).
[57] Seifert, Berndl, and Lipowsky, "Shape transformations of vesicles: Phase diagram for spontaneous- curvature and bilayer-coupling models." Physical review. A, Atomic, molecular, and optical physics **44 2**, 1182–1202 (1991).
[58] Morgan Chabanon and Padmini Rangamani, "Gaussian curvature directs the distribution of spontaneous curvature on bilayer membrane necks," Soft matter **14**, 2281–2294 (2018).
[59] Manfredo P Do Carmo, *Differential geometry of curves and surfaces: revised and updated second edition* (Courier Dover Publications, 2016).
[60] Patricia Bassereau, Rui Jin, Tobias Baumgart, Markus Deserno, Rumiana Dimova, Vadim A Frolov, Pavel V Bashkirov, Helmut Grubmüller, Reinhard Jahn, H Jelger Risselada, *et al.*, "The 2018 biomembrane curvature and remodeling roadmap," Journal of physics D: Applied physics **51**, 343001 (2018).
[61] David Tareste and Aurélien Roux, "Common energetic and mechanical features of membrane fusion and fission machineries," in *Physics of Biological Membranes* (Springer, 2018) pp. 421–469.
[62] Aurélien Roux, Gerbrand Koster, Martin Lenz, Benoît Sorre, Jean-Baptiste Manneville, Pierre Nassoy, and Patricia Bassereau, "Membrane curvature controls dynamin polymerization," Proceedings of the National Academy of Sciences **107**, 4141–4146 (2010).
[63] Daniel M Anderson, Geoffrey B McFadden, and Adam A Wheeler, "Diffuse-interface methods in fluid mechanics," Annual review of fluid mechanics **30**, 139–165 (1998).
[64] F Magaletti, Francesco Picano, M Chinappi, Luca Marino, and Carlo Massimo Casciola, "The sharp-interface limit of the cahn–hilliard/navier–stokes model for binary fluids," Journal of Fluid Mechanics **714**, 95–126 (2013).
[65] Pierre Hansen and Brigitte Jaumard, "Cluster analysis and mathematical programming," Mathematical programming **79**, 191–215 (1997).
[66] Itziar Frades and Rune Matthiesen, "Overview on techniques in cluster analysis," Bioinformatics methods in clinical research , 81–107 (2010).
[67] Abdou Rachid Thiam, Robert V Farese Jr, and Tobias C Walther, "The biophysics and cell biology of lipid droplets," Nature reviews Molecular cell biology **14**, 775–786 (2013).
[68] Gerald G Fuller and Jan Vermant, "Complex fluid-fluid interfaces: rheology and structure," Annual review of chemical and biomolecular engineering **3**, 519–543 (2012).
[69] Xiaoqiang Wang, "Asymptotic analysis of phase field formulations of bending elasticity models," SIAM J. Math. Anal. **39**, 1367–1401 (2008).
[70] Qiang Du and Lei Zhang, "A constrained string method and its numerical analysis," Communications in Mathematical Sciences **7**, 1039–1051 (2009).
[71] Shrirang Abhyankar, Jed Brown, Emil M. Constantinescu, Debojyoti Ghosh, Barry F. Smith, and Hong Zhang, *PETSc/TS: A Modern Scalable ODE/DAE Solver Library*, Tech. Rep. (2018) arXiv:1806.01437.

Supplementary Files

This is a list of supplementary files associated with this preprint. Click to download.

- SupplementaryInformationFINAL.pdf